International Journal of Heat and Mass Transfer 159 (2020) 120079

Contents lists available at ScienceDirect

International Journal of Heat and Mass Transfer

journal homepage: www.elsevier.com/locate/hmt

Technical Note

Geometric-confinement suppression of flow-boiling instability using perforated wick: Part II CHF limits and wick properties

Júlio Ferreira, Massoud Kaviany*

Department of Mechanical Engineering, University of Michigan, Ann Arbor, MI 48109, USA

ARTICLE INFO

Article history:
Received 12 May 2020
Accepted 13 May 2020
Available online 1 July 2020

Keywords:
Flow boiling
Extreme heat flux
Perforated canopy wick with levees
Hydrodynamic instability
Geometric confinement
Critical heat flux
Heat transfer coefficient

ABSTRACT

Flow-boiling canopy wick allows for control of the liquid and vapor tracks adjacent to the heated surface. Various CHF limits and the wick properties used in Part I of this two-part article are presented here.

© 2020 Elsevier Ltd. All rights reserved.

Introduction

In Part I, using a perforated wick (i.e., flow-boiling canopy wick with levees) the enhancement of the CHF and thermal conductance of the saturated (1 atm) water flow boiling were predicted and presented [1]. In this short communication (Part II), the various CHF limits used there, as well as the wick properties and its geometric optimization are presented and discussed. The CFD considerations and the choice of the VOF method for the two-phase flow calculations are discussed. The CHF and thermal conductance results for FC-72 as the fluid (saturated under 1 atm), are also predicted. The Nomenclature defining all the symbols is given in Part I.

1. Calculation of lift-off CHF

The lift-off CHF [2] calculation uses the separated flow model in which the velocity of each phase is a function of the imposed heat flux, i.e.,

$$u_g = \frac{qz}{\rho_g \delta (c_{p,l}\Delta T_{sub} + \Delta h_{lg})}, \tag{1}$$

$$u_l = \frac{u_{l,o}H}{H-\delta}\frac{qz}{\rho_l (H-\delta)(c_{p,l}\Delta T_{sub} + \Delta h_{lg})}, \tag{2}$$

where δ is the thickness of the vapor layer. The momentum equation for each phase is

$$\dot{m}^2 \frac{d}{dz}\left[\frac{(1-x)^2}{\rho_l(1-\alpha)}\right] = -(1-\alpha)\frac{dp}{dz} - \frac{\tau_{w,l}P_l}{A} - \frac{\tau_i P_i}{A} - \rho_l(1-\alpha)g\sin\theta, \tag{3}$$

$$\dot{m}^2 \frac{d}{dz}\left[\frac{x^2}{\rho_g \alpha}\right] = -\alpha\frac{dp}{dz} - \frac{\tau_{w,g}P_g}{A} - \frac{\tau_i P_i}{A} - \rho_g \alpha g\sin\theta, \tag{4}$$

where quality is defined as $x = \rho_g u_g \alpha/\dot{m}$, void fraction $\alpha = \delta/H$, P_i is the interfacial perimeter between the phases, and P_l and P_g are the perimeters of wall contact with liquid and gas phases.

Equation (4) is rearranged in the form of a pressure gradient for the gas phase

$$-\frac{dp_g}{dz} = \frac{\dot{m}^2}{\alpha}\frac{d}{dz}\left(\frac{x^2}{\alpha\rho_g}\right) + \frac{\tau_{w,g}}{\alpha}\left(\frac{1}{H} + \frac{2}{W}\alpha\right) + \frac{\tau_i}{\alpha H} + \rho_g g\sin\theta. \tag{5}$$

Combining Eqs. (3) and (4) yields the pressure gradient

$$-\frac{dp}{dz} = \frac{\dot{m}^2}{\alpha}\frac{d}{dz}\left[\frac{x^2}{\alpha\rho_g} + \frac{(1-x)^2}{(1-\alpha)\rho_l}\right] + \frac{\tau_{w,g}}{\alpha}\left(\frac{1}{H} + \frac{2}{W}\alpha\right) + \frac{\tau_{w,l}}{\alpha}\left[\frac{1}{H} + \frac{2}{W}(1-\alpha)\right] + \rho g\sin\theta. \tag{6}$$

The wall shear stress terms are expressed in terms of friction factor

$$\tau_{w,k} = \frac{1}{2}\rho_k u_k^2 \frac{f_k}{4}, \tag{7}$$

* Corresponding author.
E-mail address: kaviany@umich.edu (M. Kaviany).

https://doi.org/10.1016/j.ijheatmasstransfer.2020.120079
0017-9310/© 2020 Elsevier Ltd. All rights reserved.

where index k indicates the phase, and the friction factor is

$$f_k = 0.184\left(\frac{\rho_k u_k D_{h,k}}{\mu_k}\right)^{-1/5}. \quad (8)$$

The interfacial shear stress is

$$\tau_i = \frac{C_{f,i}}{2}\rho_g(u_g - u_l)^2, \quad (9)$$

where $C_{f,i}$ is the interfacial friction coefficient, taken as 0.5 for a wavy vapor-liquid interface. By solving Eqs. (4) and (5) along side with the velocity definitions from Eqs. (1) and (2), the variations of u_g, u_l and δ along the z direction is found.

The expression derived in [2] also considers an instability wavelength of the idealized liquid-vapor interface, similar to [3],

$$q_{CHF,ps} = \rho_g(c_{p,l}\Delta T_{sub} + \Delta h_{lg})\left[\frac{4\pi\sigma b\sin(b\pi)}{\rho_g}\right]^{1/2}\frac{\delta^{1/2}}{\lambda_c}\Big|_{z^*}, \quad (10)$$

where, the critical vapor wavelength λ_c at CHF occurs when the vapor momentum generated overcomes the interfacial pressure force, causing the wetting front to be lifted from the heated surface. The critical wavelength is

$$\lambda_c = 2\pi\left[\frac{\rho_l'\rho_g'(u_g-u_l)^2}{2\sigma(\rho_l'+\rho_g')} + \left\{\left[\frac{\rho_l'\rho_g'(u_g-u_l)^2}{2\sigma(\rho_l'+\rho_g')}\right]^2\frac{(\rho_l-\rho_g)g\cos\theta}{\sigma}\right\}^{1/2}\right]^{-1}, \quad (11)$$

where $\rho_k' = \rho_k\coth(\kappa H_k)$, the modified density of phase k.

The length of the wetting region before the interfacial lift-off is $z^* = z_o + \lambda_c(z^*)$, where z_o is the location where the relative velocity is zero. These lenghts are depicted in Part I Fig. 2(b). The CHF is calculated from the limiting condition of this force balance.

In [4], the interfacial lift-off model is implemented considering the Helmholtz wavelength perpendicular to the horizontal surface. The liquid supply to the heated surface is provided between the vapor jets in each unit cell, similar to the Zuber pool boiling instabilities. The velocity difference between ascending vapor and descending liquid leads to the Helmholtz instability

$$u_{g,n} - u_{l,n} = \left[\left(\frac{\rho_l + \rho_g}{\rho_l\rho_g}\right)\frac{2\pi\sigma}{\lambda_H}\right]^{1/2}, \quad (12)$$

where the wavelength is related to the jet diameter as $\lambda_H = \pi D = \pi\lambda_c/2$ velocities relationship is derived from the continuity as

$$u_{l,n} = \frac{\rho_g}{\rho_l}\left(\frac{\pi}{16-\pi}\right)u_{g,n}. \quad (13)$$

The rising vapor velocity is related to the CHF as

$$u_{g,n} = 16\frac{q_{CHF,ps}}{\pi\rho_g\Delta h_{lg}}. \quad (14)$$

Combining these results

$$q_{CHF,ps} = \frac{\pi\rho_g\Delta h_{lg}}{16}\left(\frac{4\sigma}{\lambda_c}\right)^{1/2}\left(\frac{\rho_l+\rho_g}{\rho_l\rho_g}\right)\left[1 + \frac{\rho_g}{\rho_l}\left(\frac{\pi}{16-\pi}\right)\right]^{-1}. \quad (15)$$

While the former model was not able to predict the CHF for plain surface for water at lower velocities, the latter has been in Section 6. Both models were used to predict the CHF for plain surface for FC-72 in Part I Subsection 6.1.

2. CHF limits

Traditionally, the concept of CHF is associated with the boiling crisis event where vapor generation prevents wetting of the heated surface. In flow boiling, however, this concept is extended as the heat transfer can now be limited by different events, some of the most relevant are shown in Part I Fig. 3. The calculated limits for saturated water at 1 atm are shown in Part I Fig. 17. The maximum theoretical heat flux is defined as [5]

$$q_{max} = \rho_g\Delta h_{lg}\left(\frac{k_B T_{lg}}{2\pi M}\right)^{1/2}. \quad (16)$$

The compressibility limit is calculated by setting $\mathrm{Ma}_{g,per} = 0.3$ [6]

$$q_{CHF,Ma} = \rho_g\Delta h_{lg}\frac{A_{per}}{A_m}u_a\mathrm{Ma}_{g,per}, \quad (17)$$

where u_a is the vapor speed of sound.

The superheating limit is calculated with volume-averaged monolayer properties as follows

$$q_{CHF,sh} = \frac{\langle k\rangle_m}{\langle\delta\rangle_m}\Delta T_{sh,max} = \frac{G}{A}\Delta T_{sh,max}, \quad (18)$$

where the maximum critical superheat $\Delta T_{sh,max}$ depends on the critical nucleation site radius [7]

$$\Delta T_{sh,max} = \frac{T_{lg}}{\Delta h_{lg}\rho_g}\left(\frac{2\sigma}{r_n} - p_{c,max}\right), \quad (19)$$

where r_n is the nucleation radius. For smooth surfaces, Marcus (1972) [7] uses nucleation theory to predict $r_n = 1.23$ μm and $\Delta T_{sh,\max} = 22$ K. Dunn and Reay (1982) [8] suggest the range $0.1\,\mu\mathrm{m} < r_n < 25\,\mu\mathrm{m}$. In the monolayer, copper particles are oxidized for improved wetting and superheating up to 75 K was observed [9]. The value shown in Part I Table 3 was calculated with $r_n = 0.2$ μm.

The choking limit is represented by the occurrence of sonic flow through a contraction, it is [10]

$$q_{CHF,ch} = c_d\frac{A_{per}}{A_m}\Delta h_{lg}\left[\gamma\rho_g p_g\left(\frac{2}{\gamma+1}\right)^{(\gamma+1)/(\gamma-1)}\right]^{1/2}, \quad (20)$$

where c_d is the discharge coefficient, γ the heat capacity ratio, and p_g the vapor pressure.

The Zuber hydrodynamic limit for pool boiling [11] is given by

$$q_{CHF,Z} = \frac{\pi}{24}\rho_g^{1/2}\Delta h_{lg}[\sigma g(\rho_l-\rho_g)]^{1/4}\frac{3}{\lambda_m^{1/2}}\left[\frac{\sigma}{g(\rho_l-\rho_g)}\right]^{1/4}, \quad (21)$$

where the wavelength λ_m can be modulated by controlling the porous surface [3].

3. Effective properties of wicks

The monolayer performance is heavily dependent on the working fluid. We must know the behavior of monolayer effective properties (namely capillary pressure, thermal conductivity and permeability) in order to properly assess the FBCW performance. The capillary pressure can be derived with the aid of Surface Evolver [12] according to the following expression

$$p_{c,max} = \frac{p_c^*\sigma\cos(\theta_c)}{d_m}. \quad (22)$$

The variation of capillary pressure with average meniscus height is shown in Fig. 1(a) for water. The maximum capillary pressure is 16.2 kPa with $p_c^* = 19$ [13]. The permeability of the monolayer is

$$K_m = \frac{\mu_l\langle u_l\rangle}{-\frac{dp}{dx}}, \quad (23)$$

and for the monolayer the meniscus topology found from the Surface Evolver code is imported into the Star-CCM+ code [14] to calculate the permeability. Fig. 1(b) shows the liquid streamlines for the close packed monolayer and variation of the permeability with

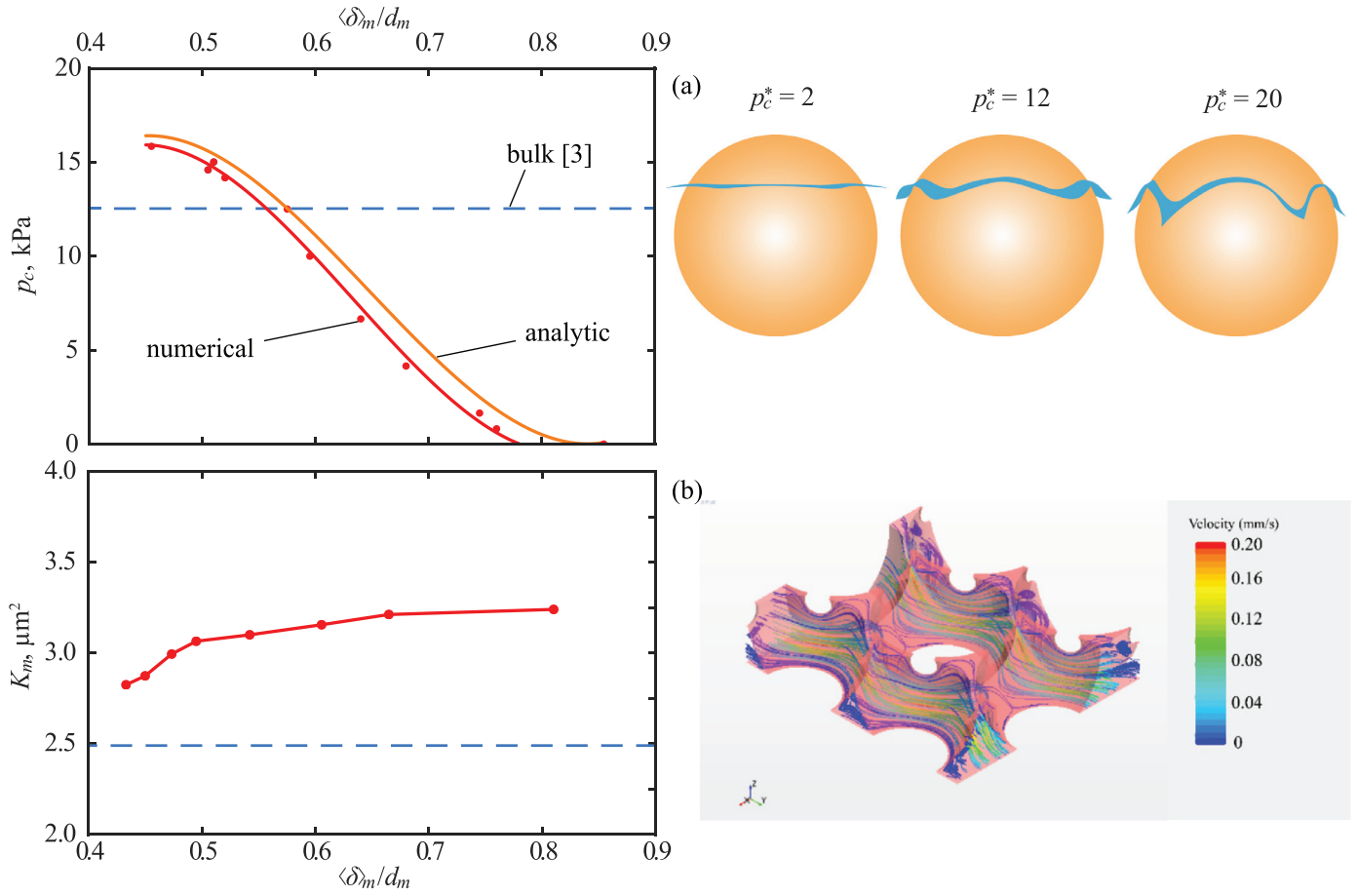

Fig. 1. (a) Variations of the capillary pressure with the meniscus thickness. Both analytical and numerical are shown. (b) Variations of monolayer permeability with respect to $\langle\delta\rangle_m$. The results are for water and parameters shown in Part I Table 3.

the meniscus thickness. The bulk permeability of Carman–Kozeny [15] gives a similar result

$$K_i = \frac{\epsilon_i^3 d_m^2}{180(1-\epsilon_i)^2}, \tag{24}$$

where ϵ_i is the porosity of the wick component i and d_m the particle diameter. The maximum particle Reynolds number is less than 0.1, confirming the suitability of the Darcy model. The porosity for canopy, posts and monolayer is listed in Part I Table 3, while d_m is the same.

To find the average pressure drop in the monolayer we start by integrating Eq. (23) using an area-averaged permeability

$$\Delta p_m = \frac{\mu_l \langle u_l \rangle}{\langle K_m \rangle} l_w, \tag{25}$$

where l_w is the average wicking length. To find the average velocity, we use the heat of evaporation

$$\langle u_l \rangle = \frac{qA_m}{\rho_l \Delta h_{lg} A_{flow}}, \tag{26}$$

where $A_m = \pi {L'_p}^2/4$ and $A_{flow} = \pi \langle\delta\rangle_m (L'_p + D_p)/2$, with L'_p as the monolayer equivalent diameter. Combining these, we have

$$\Delta p_m = \frac{\mu_l}{\rho_l \Delta h_{lg}} \left[\frac{(L'_p - D_p)/3}{\langle K_m \rangle} \frac{4{L'_p}^2}{\langle\delta\rangle_m (L'_p + D_p)/2} \right] q_{CHF,c-v}. \tag{27}$$

Similarly, Fig. 2 shows the variations of the capillary pressure and the monolayer effective thermal conductivity with the average meniscus height for FC-72. The Hadley [15,16] correlation is used for the effective thermal conductivity and the value is shown in Fig. 2(b).

4. FBCW geometry optimization

Part I Fig. 5(b) shows the variations of $q_{CHF,\,c\text{-}v}$ with respect to $N_{p,x}$ and L_{per} for different Δ_p, and $q_{CHF,\,c\text{-}v}$ increases with $N_{p,x}$ and decreases with Δ_p. By increasing the number of posts (or L_{per}), the pressure drop due vapor passing through the perforation decreases, as well as the pressure drop across the posts, allowing for the limitation to shift back to the monolayer pressure drop.

The optimized geometry for the FBCW unit cell is also shown in Part I Fig. 5(b). The wicking length is related to the aspect ratio $\gamma = W_{per}/\Delta_p$ for the anisotropic distribution of posts. The adopted geometry corresponds to an aspect ratio $\gamma = 3$. After the geometric optimization, the radial variation of monolayer meniscus thickness (due to the variation in the capillary pressure), surface superheat temperature, and thermal conductance found from the resistance network models and are shown in Fig. 3(a) to (c). The results are for $q_{CHF} = 15$ MW/m^2 for water. The area-averages (annulus) are also shown, they are calculated as

$$\langle\phi\rangle = \frac{\sum \phi_i A_{h,i}}{\sum A_{h,i}}, \tag{28}$$

where ϕ_i is the variable of interest and $A_{h,i}$ the discrete heated (annulus) area.

5. CFD and VOF validations

Wick: The monolayer liquid meniscus topology is obtained from Surface Evolver energy minimization code [12]. Then the direct (pointwise conservation equations) numerical simulation with

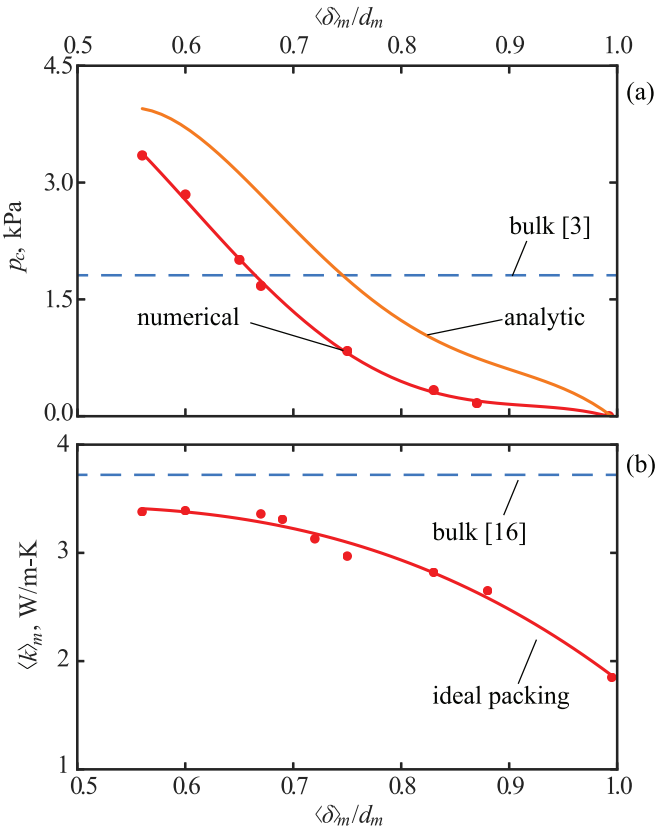

Fig. 2. Variations of (a) capillary pressure, and (b) monolayer effective thermal conductivity with respect to normalized (using sintered particle diameter) average meniscus thickness with ideal packing and bulk properites [16], for FC-72. For the capillary pressure, both the numerical and analytical results are shown.

Star-CCM+ solver [14] is used for the monolayer permeability and effective conductivity using the resulting topology from Surface Evolver code. The resistance network model solves momentum and mass conservation in the wick while incorporating the meniscus thickness dependence.

Channel: For the two-phase flow the pointwise conservation equation, commercial solver ANSYS Fluent [17] is used with following options: fluid-fluid; transient, incompressible, isothermal, turbulent flow (realizable $k-\epsilon$ closure model), first order implicit time, explicit volume of fluid (VOF) [18] with geometric reconstruction (Courant <0.25), the SIMPLE scheme with single momentum and continuity equation, and mesh resolution ≈ 0.25 mm. The VOF method is preferred over the level-set method because of its mass conservation characteristics [19].

The pointwise Fluent continuity and momentum equations are:

$$\frac{\partial \rho}{\partial t}+\nabla\cdot\boldsymbol{u}=0, \tag{29}$$

$$\tfrac{\partial}{\partial t}(\rho\boldsymbol{u})+\nabla\cdot(\rho\boldsymbol{u}\boldsymbol{u})=-\nabla p+\nabla\cdot\left[\mu(\nabla\boldsymbol{u}+\nabla\boldsymbol{u}^{T})\right]+\rho\boldsymbol{g}+\boldsymbol{f}_s, \tag{30}$$

$$\frac{\partial}{\partial t}(\alpha\rho_g)+\nabla\cdot(\alpha\rho_g\boldsymbol{u}_g)=0, \tag{31}$$

$$\rho=\alpha\rho_g+(1-\alpha)\rho_l, \tag{32}$$

$$\mu=\alpha\mu_g+(1-\alpha)\mu_l, \tag{33}$$

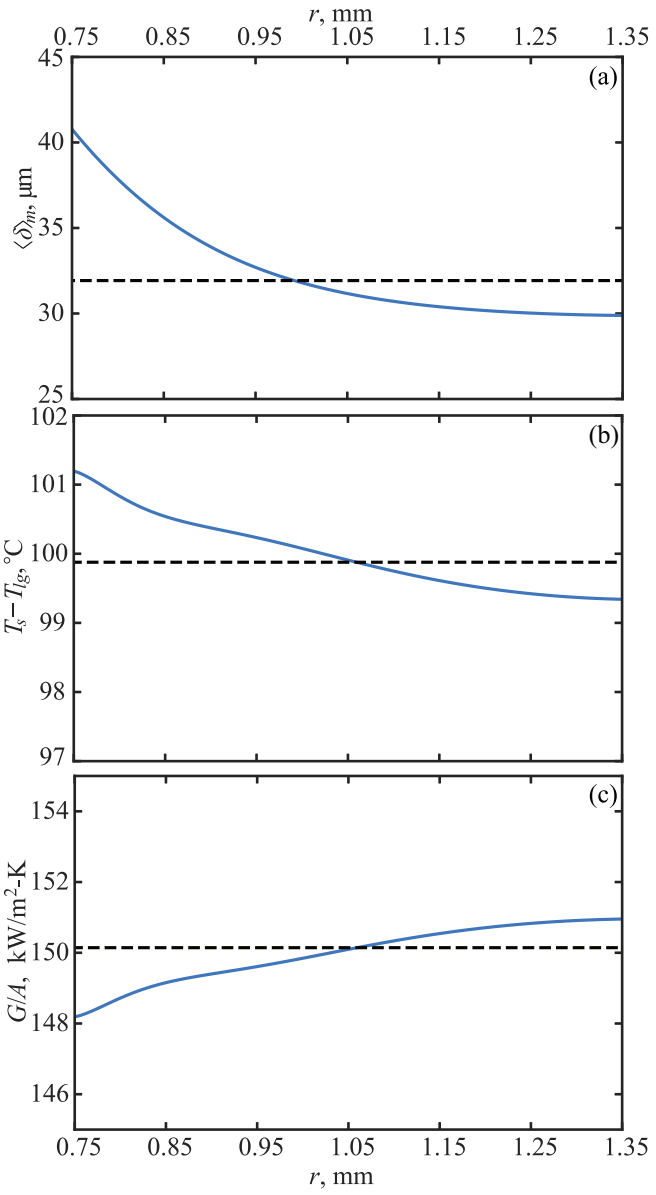

Fig. 3. Radial distributions of the monolayer variables calculated using the network model for water: (a) meniscus thickness $\langle\delta\rangle_m$, superheat T_s-T_{lg}, and (c) thermal conductance G/A for $q=15$ MW/m^2. Dashed line represents the area-weighted average.

$$\boldsymbol{f}_s=\sigma\frac{\rho\kappa_g\nabla\alpha}{(\rho_g+\rho_l)/2}. \tag{34}$$

Declaration of Competing Interest

The authors declare that they have no known competing financial interests or personal relationships that could have appeared to influence the work reported in this paper.

CRediT authorship contribution statement

Júlio Ferreira: Formal analysis, Visualization, Writing - original draft. **Massoud Kaviany:** Conceptualization, Data curation, Supervision, Project administration.

Acknowledgements

This work is supported by NSF - USA (Thermal Transport and Processes, CBET16235720). JF is thankful and acknowledges his scholarship supported by CAPES - Brazilian Federal Agency for Support and Evaluation of Graduate Education within the Ministry of Education. We are thankful to Minki Kim for his technical guidance.

References

[1] J. Ferreira, M. Kaviany, Geometric-confinement Suppresion of Flow-boiling Instability Using Perforated Wick: Part I CHF and Conductance Enhancement, Int. J. Heat Mass Transf. 159 (2020) 120080.
[2] J. Sturgis, I. Mudawar, Critical heat flux in a long, rectangular channel subjected to one-sided heating-II. analysis of critical heat flux data, Int. J. Heat Mass Transf. 42 (10) (1999) 1849–1862, doi:10.1016/S0017-9310(98)00275-0. http://www.sciencedirect.com/science/article/pii/S0017931098002750
[3] S.G. Liter, M. Kaviany, Pool-boilingCHF enhancement by modulated porous-layer coating: theory and experiment, Int. J. Heat Mass Transf. 44 (22) (2001) 4287–4311, doi:10.1016/S0017-9310(01)00084-9. http://www.sciencedirect.com/science/article/pii/S0017931001000849
[4] C.-N. Huang, C.R. Kharangate, A new mechanistic model for predicting flow boiling critical heat flux based on hydrodynamic instabilities, Int. J. Heat Mass Transf. 138 (2019) 1295–1309, doi:10.1016/j.ijheatmasstransfer.2019.04.103. http://www.sciencedirect.com/science/article/pii/S001793101930167X
[5] W.R. Gambill, J.H. Lienhard, An upper bound for the critical boiling heat flux, J. Heat Transf. 111 (3) (1989) 815–818, doi:10.1115/1.3250759.
[6] P.K. Kundu, I.M. Cohen, D.R. Dowling (Eds.), Chapter 15 - Compressible Flow, Academic Press, Boston, 2012. Fluid Mechanics, 5th Edition, pp. 729–778, doi:10.1016/B978-0-12-382100-3.10015-0.
[7] B.D. Marcus, Theory and design of variable conductance heat pipes, 1972, https://ntrs.nasa.gov/archive/nasa/casi.ntrs.nasa.gov/19720016303.pdf. Tech. rep., Washington D.C.
[8] P. Dunn, D.A. Reay, Chapter 2 - Theory of the Heat Pipe, in: P. Dunn, D.A. Reay (Eds.), Heat Pipes, 3rd, Pergamon, Oxford, 1982, pp. 23–89, doi:10.1016/B978-0-08-029355-4.50008-5.
[9] G. Hwang, E. Fleming, B. Carne, S. Sharratt, Y. Nam, P. Dussinger, Y. Ju, M. Kaviany, Multi-artery heat-pipe spreader: lateral liquid supply, Int. J. Heat Mass Transf. 54 (11) (2011) 2334–2340, doi:10.1016/j.ijheatmasstransfer.2011.02.029. http://www.sciencedirect.com/science/article/pii/S0017931011000846
[10] D.W. Green, R.H. Perry, Perry's Chemical Engineer, Handbook, 8th, McGraw-Hill, 2007.
[11] N. Zuber, Hydrodynamic aspects of boiling heat transfer, University of California, Los Angeles, 1959 Ph.D. thesis.
[12] K.A. Brakke, The surface evolver, Exp. Math. 1 (2) (1992) 141–165, doi:10.1080/10586458.1992.10504253.
[13] S. Modak, M. Kaviany, S. Hoenig, R. Bonner, Numerical analysis of meniscus dynamics in monolayer-wick dropwise condensation, Numer. Heat Transf. Part A: Appl. 76 (5) (2019) 301–322, doi:10.1080/10407782.2019.1627829.
[14] Siemens, STAR-CCM+ user manual, 2020,
[15] M. Kaviany, Principles of Heat Transfer in Porous Media, 2nd, Springer, 1995.
[16] G. Hadley, Thermal conductivity of packed metal powders, Int. J. Heat Mass Transf. 29 (6) (1986) 909–920, doi:10.1016/0017-9310(86)90186-9. http://www.sciencedirect.com/science/article/pii/0017931086901869
[17] ANSYS, Fluent reference manual, 2009,
[18] Y. Li, K. Alame, K. Mahesh, Feature-resolved computational and analytical study of laminar drag reduction by superhydrophobic surfaces, Phys. Rev. Fluids 2 (2017) 054002, doi:10.1103/PhysRevFluids.2.054002.
[19] S. Mirjalili, S. Jain, M. Dodd, Interface-capturing methods for two-phase flows: an overview and recent developments, in: Center for Turbulence Research - Annual Research Brief, 2017, pp. 117–135.